PLOS BIOLOGY

SHORT REPORTS

The activation cascade of the broad-spectrum antiviral bemnifosbuvir characterized at atomic resolution

Aurélie Chazot[1], Claire Zimberger[1], Mikael Feracci[1], Adel Moussa[2], Steven Good[2], Jean-Pierre Sommadossi[2], Karine Alvarez[1], François Ferron[1,3]*, Bruno Canard[1,3]*

1 Aix Marseille Université, CNRS, AFMB, UMR 7257, Marseille, France, **2** ATEA Pharmaceuticals, Inc., Boston, Massachusetts, United States of America, **3** European Virus Bioinformatics Center, Jena, Germany

* francois.ferron@univ-amu.fr (FF); bruno.canard@univ-amu.fr (BC)

Citation: Chazot A, Zimberger C, Feracci M, Moussa A, Good S, Sommadossi J-P, et al. (2024) The activation cascade of the broad-spectrum antiviral bemnifosbuvir characterized at atomic resolution. PLoS Biol 22(8): e3002743. https://doi.org/10.1371/journal.pbio.3002743

Academic Editor: Chaitan Khosla, Stanford University, UNITED STATES OF AMERICA

Received: February 19, 2024

Accepted: July 9, 2024

Published: August 27, 2024

Data Availability Statement: The coordinates and structure factors for HINT1, ADALP1, GUK1, and NDPK structures have been deposited in the PDB with accession codes 8PWK, 8QCH, 8PTS, and 8PIE, respectively. Structural data can be found at https://doi.org/10.2210/pdb8pwk/pdb, https://doi.org/10.2210/pdb8qch/pdb, https://doi.org/10.2210/pdb8pts/pdb and https://doi.org/10.2210/pdb8pie/pdb. The data underlying figures, supplementary figures, and tables, including the raw blots for S2 Fig, can be found at https://zenodo.org/records/12606239.

Abstract

Bemnifosbuvir (AT-527) and AT-752 are guanosine analogues currently in clinical trials against several RNA viruses. Here, we show that these drugs require a minimal set of 5 cellular enzymes for activation to their common 5′-triphosphate AT-9010, with an obligate order of reactions. AT-9010 selectively inhibits essential viral enzymes, accounting for antiviral potency. Functional and structural data at atomic resolution decipher N^6-purine deamination compatible with its metabolic activation. Crystal structures of human histidine triad nucleotide binding protein 1, adenosine deaminase-like protein 1, guanylate kinase 1, and nucleoside diphosphate kinase at 2.09, 2.44, 1.76, and 1.9 Å resolution, respectively, with cognate precursors of AT-9010 illuminate the activation pathway from the orally available bemnifosbuvir to AT-9010, pointing to key drug–protein contacts along the activation pathway. Our work provides a framework to integrate the design of antiviral nucleotide analogues, confronting requirements and constraints associated with activation enzymes along the 5′-triphosphate assembly line.

Introduction

The recent Coronavirus Disease 2019 (COVID-19) crisis due to Severe Acute Respiratory Syndrome Coronavirus 2 (SARS-CoV-2) has evidenced the need for safe and potent antivirals, in conjunction with accurate and rapid diagnostics. First, at the public level, prophylaxis around index cases may significantly curb emergence by cutting viral load and transmissibility. Second, at the individual level, early therapy may limit virus spread to vital organs, avoiding complications.

Nucleoside/nucleotide analogues (NAs) represent the first family of compounds that have been used as direct-acting antivirals several decades ago [1–3] against DNA viruses such as herpesvirus, hepatitis B virus (HBV), the retrovirus human immunodeficiency virus type 1 (HIV-1), and RNA viruses such as hepatitis C virus (HCV) and SARS-CoV-2. Upon reaching their target cells, antiviral drugs often act after intracellular activation. Early biologically active nucleoside analogues (NAs) such as ara-C (cytarabine) penetrate the target cell efficiently and

Funding: This project has received funding through the 2023 Louis Pasteur Bicentenary Prize, the Grand Prix Scientifique de la Fondation Simone et Cino Del Duca – Institut de France awarded to La Fondation CNRS for BC, and Research-Action-ANR Covid-19 -PHOTONS (2020-2022)-PHOsphorylation Tools for Nucleotides Synthesis awarded to KA. AC received a doctoral fellowship from the Ministère de l'Education Nationale, de l'Enseignement Supérieur et de la Recherche. This work was supported by the 'Agence Nationale pour la Recherche' through the French Infrastructure for Integrated Structural Biology (FRISBI) [ANR-10-INSB-05-01].The funders had no role in study design, data collection and analysis, decision to publish, or preparation of the manuscript.

Competing interests: S.G., A.M. and J.P.S. are employees of ATEA Pharmaceuticals, Inc.

Abbreviations: ADALP1, adenosine deaminase-like protein 1; CatA, Cathepsin A; CES1, carboxylesterase 1; COVID-19, Coronavirus Disease 2019; GUK1, guanylate kinase 1; HBV, hepatitis B virus; HCV, hepatitis C virus; HINT, histidine triad nucleotide-binding protein; HIV-1, human immunodeficiency virus type 1; NA, nucleoside/nucleotide analogue; NDPK, nucleoside diphosphate kinase; RdRp, RNA-dependent RNA polymerase; RDV, remdesivir; SARS-CoV-2, Severe Acute Respiratory Syndrome Coronavirus 2; SOF, sofosbuvir; TAF, tenofovir alafenamide; TEAB, triethylammonium bicarbonate.

are transformed into the nucleoside analogue 5′-triphosphate (NA-TP) by a series of kinase reactions (reviewed in [2–4]).

ProTide prodrug technology has been implemented to deliver NA carrying a 5′-phosphate or phosphonate [5]. Aryloxy phosphoramidate prodrugs of, e.g., tenofovir alafenamide (TAF) for HIV-1 and HBV, sofosbuvir (SOF) for HCV, and remdesivir (RDV) for SARS-CoV-2 have met clinical success [5–7]. They achieve cell penetration through shielding the phosphate charges, and preferential hydrolysis at the P-N bond bypasses the first—often limiting—nucleoside kinase reaction, allowing significant building up of NA-TP pools. NA-TPs poison viral RNA synthesis specifically, provoking premature viral RNA chain termination or chemical/genetic corruption of the viral nucleic acid [8].

Two main parameters determine NA potency: the concentration ratio of NA-TP over its natural NTP competitor, and the selectivity of the viral RNA-dependent RNA polymerase (RdRp) for use of the NA-TP [9]. NA-TP pools must be formed efficiently upon intracellular activation, and the differences of the NA-TP scaffold relative to its natural NTP counterpart must remain "below the radar" of the viral RdRp.

General knowledge, structural and functional data about cellular enzymes along a given NA activation pathway are fragmented. Numerous NAs have been designed showing appropriate poisoning of viral RNA synthesis through their 5′-TP in vitro, but clinical development has failed for lack of transmembrane permeability, intracellular metabolic activation, and/or cellular toxicity. Clearly, NA drug-design needs an integrated view (i.e., structural, functional, and mechanistic) from the delivered NA up to the ultimate inhibited viral enzyme reaction accounting for antiviral effect, as well as the molecular basis for (non)interaction with cellular enzymes.

Such a global picture is emerging for 2 FDA-approved NA prodrugs directed against RNA viruses, SOF and RDV (S1 Fig). The activation pathway of RDV has been elucidated and profiled in a variety of tissues [10]. RDV is an aryloxy phosphoramidate prodrug (GS-5734, Veklury) converted in 2 steps to the 5′-monophosphate NA by esterases belonging to 2 families (Cathepsin A (CatA) and/or carboxylesterase 1 (CES1), followed by the cleavage of the P-N bond by a histidine triad nucleotide (HINT) phosphoramidase [11]. The resulting monophosphate NA is then converted to RDV-TP by the subsequent action of 2 cellular phosphotransferases. However, although detailed studies at the atomic level exist to understand accommodation of the 1′-CN group at the SARS-CoV-2 RdRp active site [12,13], structural insight of the relevant activation intermediates is lacking for all enzymes in the activation pathway.

SOF (PSI-7851, Sovaldi) undergoes the same CatA/CES1 deprotection pathway as RDV but is activated to the 5′-triphosphate by the UMP-CMP kinase and the nucleoside diphosphate kinase (NDPK) sequentially [14]. Here again, although the mechanism of chain-termination at the HCV NS5b RdRp has been elucidated at atomic resolution [15], the structural basis of activation remains uncharacterized.

Bemnifosbuvir (AT-527 (hemisulfate salt), AT-511 (free base)) is a guanosine analogue currently in clinical trials against SARS-CoV-2 and HCV. It showed in Phase II clinical trials a 71% risk reduction in outpatients with moderate COVID-19 (MORNINGSKY; NCT04396106) [16,17], but the associated Phase III study ended prematurely as it did not meet its primary end point [17]. It is currently under investigation in a global Phase III clinical trial in outpatients at high risk for disease progression (SUNRISE-3; NCT05629962), as well as evaluated as an anti-HCV drug [18] in combination with the NS5A inhibitor ruzasvir (NCT05904470). Its epimer AT-752 is currently in clinical Phase II against Dengue virus (NCT05466240) [19,20].

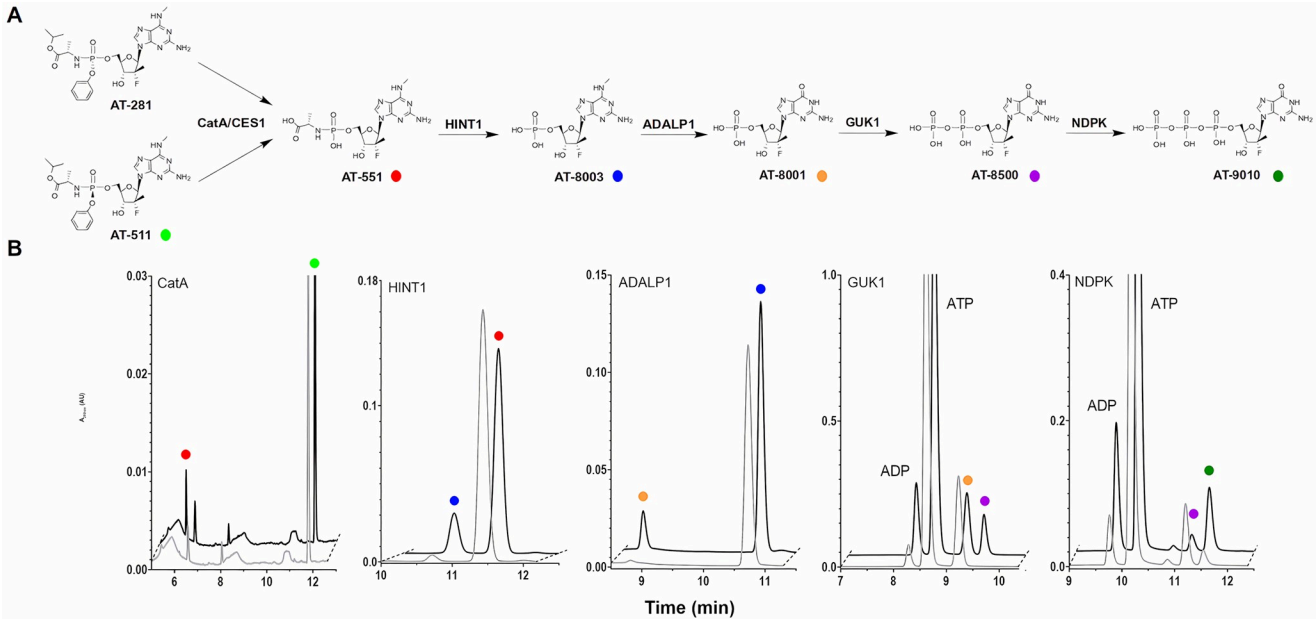

Fig 1. Validation of the activation pathway of bemnifosbuvir. (**A**) The activation pathway of AT-511, the free base form of bemnifosbuvir (AT-527), into the active form AT-9010. AT-281, the diastereoisomer of AT-511 and free base form of AT-752, follows the same pathway. (**B**) Typical RP-HPLC chromatograms of the enzymatic assays after 2 min (gray) and the last kinetic point (black). For each enzyme CatA, CES1, HINT1, ADALP1, GUK1, and NDPK, the successful validation of activity results in conversion of the substrate into the corresponding product. All compounds were identified by coinjection with authentic samples. The data underlying this figure can be found at https://zenodo.org/records/12606239. ADALP1, adenosine deaminase-like protein 1; CatA, Cathepsin A; CES1, carboxylesterase 1; GUK1, guanylate kinase 1; HINT1, histidine triad nucleotide-binding protein type 1; NDPK, nucleoside diphosphate kinase; RP-HPLC, reversed-phase high-performance liquid chromatography.

https://doi.org/10.1371/journal.pbio.3002743.g001

Both bemnifosbuvir and AT-752, once processed by the CatA/CES1 pathway, converge to the same precursor AT-551 (Fig 1A) [18]. These 2 analogues are among the few antiviral purine NAs devoid of significant cellular toxicity. Once the P-N bond of AT-551 is hydrolyzed (presumably) by HINT1 [21], giving rise to the monophosphate AT-8003, the diamino purine base is (presumably) converted to a natural guanosine base through specific N^6-deamination carried out by the adenosine deaminase-like protein 1 (ADALP1) enzyme [22,23]. This reaction is believed to skirt a cellular step responsible for the toxicity of unprotected, "natural" guanosine analogues [18,24]. The resulting 2′-F-2′-C-methyl guanosine 5′-monophosphate (AT-8001) is (presumably) consecutively phosphorylated twice to yield AT-9010 by means of guanylate kinase 1 (GUK1) [25] and nucleoside diphosphate kinase (NDPK) [26,27]. AT-9010 accumulates in various cell types [18]. The HCV RNA synthesis is likely halted through RNA chain termination [18]. SARS-CoV-2 RNA synthesis is halted through targeting of the replicase complex at 2 distinct sites [28], and the Dengue virus RNA synthesis is also halted through targeting 2 sites of the NS5 protein [19,20].

Most information relative to activation pathways has been obtained through measurements of intracellular concentrations of NA intermediates [10,11,14,24]. Studies described herein aim to ascertain which individual enzymes are involved in the activation pathway, as well as clarify their structural and functional mode of interaction with activation intermediates. Interaction maps of NAs with both activating partners and viral enzymes at atomic resolution would guide improved design of novel NAs.

In this work, we have identified a minimal set of 5 human enzymes involved in the activation of bemnifosbuvir and AT-752 to their active 5′-TP form AT-9010. We demonstrate distinct stereo-preference of CatA and CES1 for AT-527 and its epimer AT-752, respectively. We

elucidate an ordered activation pathway with potential limiting steps, including substrate specificity requirements at the N^6-purine position for ADALP1. Structural analysis with key human enzymes HINT1, ADALP1, GUK1, and NDPK in complex with the bemnifosbuvir/AT-752 intermediate NA at 2.09, 2.44, 1.76, and 1.9 Å resolution informs on both the N^6-purine and 2′-ribose chemosteric requirements leading to active NAs targeting viral RdRps.

Results

The putative metabolic pathway of AT-511 (free base form of AT-527, bemnifosbuvir) and AT-281 (free base form of AT-752) is shown in Fig 1A.

CatA and/or CES1 presumably precede a spontaneous decomposition yielding the L-alanine phosphoramidate prodrug AT-551, common to both AT-752 and AT-527 pathways. AT-551 is then subjected to 4 enzyme-mediated reactions leading to the active 5′-triphosphate form, AT-9010. Apart from the N^6-deamination reaction, this pathway has been inferred from that of the anti-HCV drug SOF, which carries a uracil base instead of the N^6-methyl diamino purine base (a guanine precursor) of either AT-752 or AT-527. The SOF pathway, however, has been determined indirectly, by measuring intermediates in cells treated with SOF [11,14].

Five enzymes are needed to convert AT-527 (bemnifosbuvir) or AT-752 to their active form AT-9010

We expressed, purified, and crystallized 4 of the human enzymes widely distributed in human tissues (https://proteinatlas.org) and supposedly involved in the prodrug activation pathway (Figs 1A and S2). Together with human enzymes CatA and CES1, we challenged HINT1, ADALP1, GUK1, and NDPK with their anticipated substrates depicted in Figs 1A and S3. We made use of an HPLC-UV method to follow the conversion of the substrate, together with a kinetic monitoring relative to known standards (Fig 1B).

Both AT-527 and AT-752 can be enzymatically converted to AT-9010 by an ordered series of reaction involving nonspecific esterases CatA/CES1, HINT1, ADALP1, GUK1, and NDPK (Table 1). For AT-511, nonspecific esterases CatA and CES1 exhibit an approximately 300-fold difference in activity, whereas hydrolysis efficiency is quite similar for AT-281 (<3-fold difference). Both for control and AT compounds, the early steps of the pathway are the slowest, with di- and triphosphate formation showing the fastest turnovers.

The phosphate stereo-selectivity of CatA/CES1 usage

The phosphorus atom of the aryloxy phosphoramidate moiety is chiral, resulting in 2 possible epimers. AT-511 (S_P isomer) is the free base form of AT-527, and AT-281 (R_P isomer) is the free base form of AT-752 (S3 Fig). As shown for SOF, the difference of antiviral activity between the 2 stereoisomers could be due to the activation of the prodrug and more specifically to the stereo-selectivity of the enzymes involved in the first hydrolytic step.

CatA or CES1 were incubated with either AT-511 or AT-281, and comparative velocities of AT-551 formation were measured (S4 Fig). CatA always shows higher activity than CES1. CatA prefers by 14-fold the S_P isomer AT-511 over the R_P isomer AT-281 (9.8 ± 0.3 versus 0.7 ± 0.1 nmol/min/nmol protein). Interestingly, however, a reversed stereo-selectivity is observed for CES1 relative to CatA: CES1 hydrolyses AT-281 approximately 10-fold faster than AT-511 (0.27 ± 0.02 versus 0.033 ± 0.004 nmol/min/nmol protein, respectively). These results align with those obtained with a variety of clinically relevant prodrugs; for SOF, TAF, and RDV, CES preferentially hydrolyzes the R_P isomer, whereas CatA prefers the S_P isomer of the aryloxy phosphoramidate moiety [10,11,14]. We conclude that nonspecific esterases of the CatA/CES1 type are able to convert bona fide McGuigan ProTides into HINT1 substrates

Table 1. Activities of enzymes involved in AT-527/AT-511 and AT-752/AT-281 activation.

Enzyme	Substrate	Specific activity (nmol.min^{-1}.nmol^{-1})[a]
CatA	**AT-511**	9.8 ± 0.3
	AT-281	0.7 ± 0.1
CES1	**AT-511**	0.033 ± 0.004
	AT-281	0.27 ± 0.02
HINT1	AMP-NH2	101 ± 8
	AT-551	0.7 ± 0.2
ADALP1	N^6-Me-AMP	42 ± 2
	AT-8003	9.4 ± 0.4
	AT-8010	5.21 ± 0.07
	AT-8004	11.9 ± 0.1
	AT-8002	0.94 ± 0.03
	AT-551	No activity
	AT-229	No activity
	AT-259	No activity
GUK1	GMP	6,800 ± 300
	AT-8001	34 ± 5
	AT-8003	No activity
NDPK	GDP	5,400 ± 800
	AT-8500	1,300 ± 100

[a]Results were obtained from at least 3 independent experiments and reported as means ± standard deviations.

https://doi.org/10.1371/journal.pbio.3002743.t001

from both AT-752 and AT-527. The respective abundance of each enzyme in cells or tissues might be useful as a predictor of ester hydrolysis efficiency in these given cells or tissues.

Specificity and order of the reactions

AT-551 could not act as a substrate for ADALP1 (S5 Fig). This result indicates that the L-alanine phosphoramidate precludes efficient either binding or catalytic conversion of AT-551 with ADALP1 (see structural data below). AT-8003 could neither be a substrate for GUK1, indicating that the N^6 position must be either unsubstituted or only an O^6 to allow binding and phosphorylation of the NMP (S5 Fig). Unless other enzymes exist that could use these substrates and bypass the proposed activation sequence, the absence of reactivity reported here is consistent with the order of the reaction pathway reported in Fig 1A.

Structural and functional analysis of HINT1 substrate specificity

HINT1 belongs to the HIT (histidine triad) protein superfamily and has been shown to hydrolyse the P-N bonds in SOF and RDV [10,11,14]. HINT1 is able to hydrolyze AMP-NH_2 (control) into AMP, and AT-551 into AT-8003 with specific activities of 101 ± 8 and 0.7 ± 0.2 nmol/min/nmol protein, respectively (Fig 1B and Table 1). HINT1 is thus approximately 140-fold faster with the control compound than with AT-551.

We crystallized HINT1 in complex with AT-551 or AT-8003 (Fig 2A–2C).

For AT-551, reaction occurred readily under either crystal soaking or co-crystallization conditions. Co-crystallization resulted in AT-8003 bound to the active site on 1 monomer (Fig 2A). The crystal structure (2.09 Å resolution) shows a homodimer, each monomer being almost perfectly superimposable (RMSD approximately 0.18 Å on the visible 126 aa).

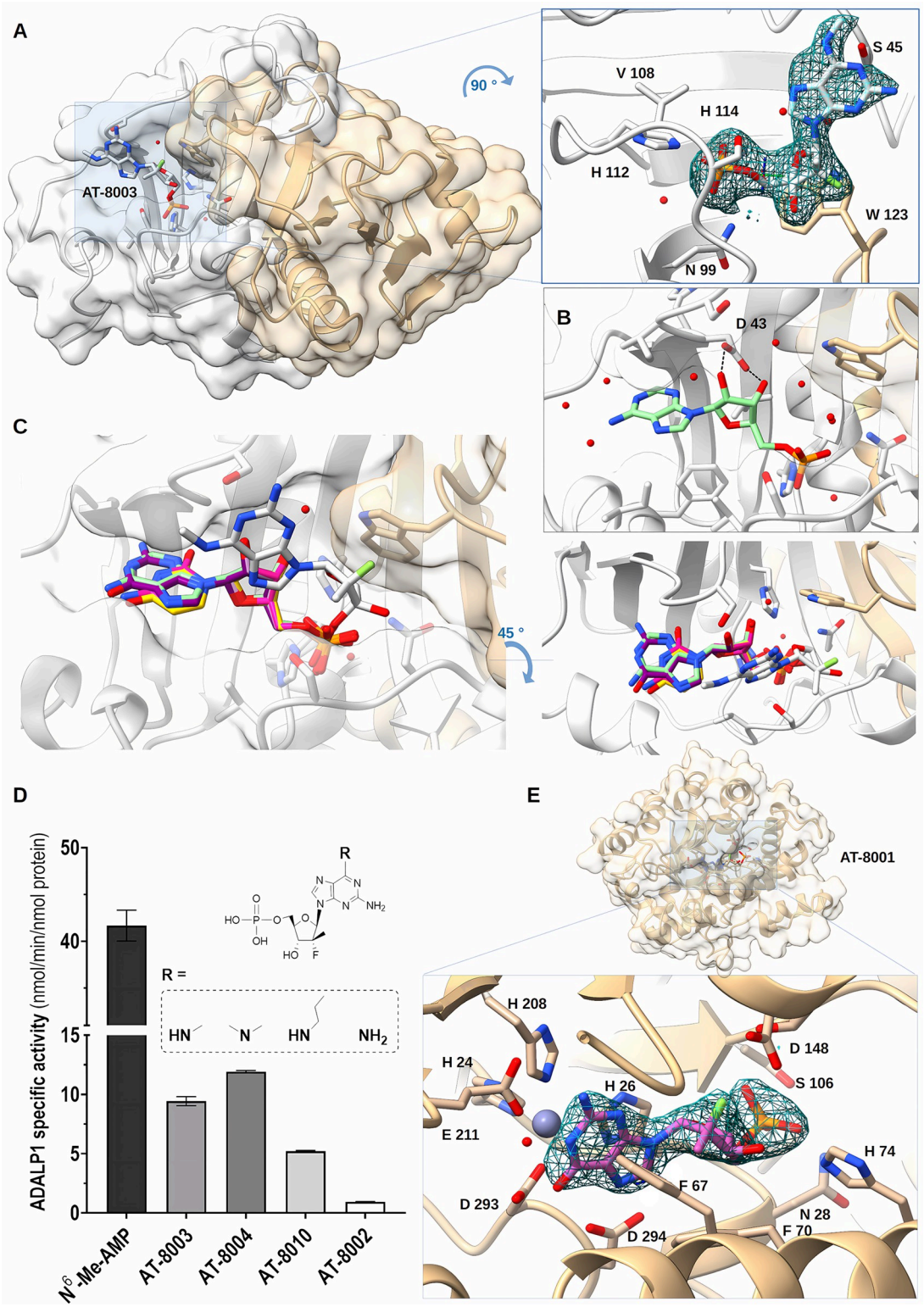

Fig 2. **(A)** Structure of human HINT1 in complex with AT-8003. Homodimer of human HINT1 structure complexed with 1 AT-8003 compound is represented in ribbon and transparent surface, while compound is represented in sticks with heteroatom colors. On the right side, an enlargement of the molecule in the active site is presented at 90˚. Side chains of interacting residues with the molecule are shown in sticks. The F_o—F_c omit map of the molecule is presented at 1 σ. **(B)** Binding mode involving direct coordination of the 2′ and 3′ O ribose of AMP (light green–PDB: 5ED6) by Asp 43. **(C)** Comparison of the relative

positions of AMP (light green–PDB: 5ED6), CMP (orange–PDB: 5KM2), UMP (yellow–PDB: 5KM3), GMP (purple–PDB: 5KM1) in respect to AT-8003 (white) in the HINT1 active site. AT-8003 is positioned almost orthogonally to other nucleotides bound in other structural models, and only the phosphate positions are undistinguishable. The right panel is the same figure turned 45˚. **(D)** Human ADALP1 analysis and specificity. Activity of ADALP1 with N^6-Me-AMP as control substrate, AT-8003 as anticipated substrate and N^6-modified analogues of AT-8003: AT-8004 with a N^6-dimethyl group, AT-8010 with a N^6-n-propyl group and AT-8002 with a N^6-amino group. About 100 nM ADALP1 (or 1 μM for AT-8002) was incubated 2 h at 37˚C with 200 μM substrate. Bars show mean values (± SD) of 3 independent experiments. **(E)** ADALP1 in complex with AT-8001. Human ADALP1 structure is represented in ribbon and transparent surface, while compound is represented in sticks with heteroatom colors. The molecule is deeply buried in a closed conformation of ADALP1. On the right side, a zoomed part of the molecule as well as the zinc ion (gray ball) is presented in the active site. Side chains of interacting residues with the molecule are shown in sticks. The F_o—F_c omit map of the molecule is presented at 1 σ. The data underlying this figure can be found at https://doi.org/10.2210/pdb8pwk/pdb and https://doi.org/10.2210/pdb8qch/pdb.

https://doi.org/10.1371/journal.pbio.3002743.g002

The bound product pose is significantly different from all existing HINT1 structures [21] in complex with AMP, GMP, or NMP-phosphoramidate ligands (Fig 2B). In all available structures so far, the NA is buried in a pocket, contacting conserved amino acids Ile 44 and Asp 43 involved in purine base stacking and ribose 2′,3′-OH ribose bi-dentate binding, respectively. Here, the methylated diamino purine base is bound outside the nucleobase binding pocket, shifted by 90˚ and making a single hydrogen bond with Ser 45 that could occur with any purine or pyrimidine base. Trp 123 is facing the ribose offering a weak hydrophobic stabilization. Remarkably, the 2 parts of the AT-8003, which differentiate it from guanosine, are not engaged in any amino acid contact. Both the N^6-amino purine and the 2′-C-methyl, 2′-F are projecting into the solvent.

The phosphate is closely superimposable to that observed in other published structures [21]. The catalytic His 112 nucleophilic nitrogen is 3.1 Å away from the phosphate, and the hydrolytic water molecule is positioned opposite to the putative leaving amine and general acid His 114 and/or His 51. In a similar complex (PDB: 5IPE), the O^6-guanine of GMP is located at 3.3 Å from the Ile 18 side chain, and there is space to accommodate an N^6-methyl amino group at the solvent–protein interface. The AT-8003 ribose pucker is of *Northern* (*N*) configuration: C3′ up and C2′ down (the *Southern* (S) pucker has the C3′ down and C2′ up), as this conformation must be imposed by the presence of its 2′-C-methyl. The ribose pucker of GMP and AMP analogues in all other structures being *S*, we surmise the 2′-C-methyl is driving this alternate preferential NA binding mode seen in all structures reported here.

Structural and functional analysis of ADALP1 substrate specificity

ADALP1 is a deaminase acting on N^6-substituted purine nucleoside monophosphates [23]. The activity of purified ADALP1 was tested on N^6-Me-AMP as a control compound before testing on the anticipated substrate AT-8003. Because the anti-HIV drug abacavir bears an N^6-cyclopropyl modification [22], we tested several N^6-modified analogues: –NH(nPr) (AT-8010), $-N(CH_3)_2$ (AT-8004), and $-NH_2$ (AT-8002). The nucleoside versions of AT-8003 and AT-8010 were also tested, i.e., AT-229 and AT-259, respectively.

ADALP1 is able to convert N^6-Me-AMP into IMP (42 ± 2 nmol/min/nmol protein), as well as AT-8003, AT-8004, and AT-8010 into AT-8001. AT-8003, AT-8004, and AT-8010 are converted 3- to 8-fold slower than N^6-Me-AMP (9.4 ± 0.4 nmol/min/nmol protein, 11.9 ± 0.1 nmol/min/nmol protein, and 5.21 ± 0.07 nmol/min/nmol protein, respectively; Fig 1B and Table 1). ADALP1 is thus able to accept the 2′-C-methyl, 2′-F modifications on the ribose part, as well as several substituents on the N^6-position. Extension of the N^6-substituent, not its bulk immediately close to the nitrogen atom, seems to negatively influence activity (Fig 2D).

Under our experimental conditions, ADALP1 converts only nucleoside monophosphate substrates: No activity was detected with the nucleosides AT-229 and AT-259.

Interestingly, the reaction is approximately 45-fold slower with AT-8002 as substrate compared to the natural substrate N^6-Me-AMP, indicating that at least one substituent on the nitrogen atom may enhance the leaving group ability.

We co-crystallized ADALP1 and AT-8003. The solved ADALP1 structure adopts an α/β-barrel architecture similar to that of ADAs [29], with the essential Zn^{2+} ion tightly bound in the vicinity of the catalytic center (Figs 2E and S6A). Fourteen α-helices surrounding 8 parallel β-strands constitute a TIM-barrel fold [30]. The asymmetric unit contains 8 copies of the protein. Since ADALP1 was purified as a homogeneous monomer (S6B Fig), the octamer likely appeared during crystallogenesis. Although ADALP1 was co-crystallized with the substrate AT-8003, the product AT-8001 was found bound at the active site. The compound is found in all 8 chains, and all the chains found in the asymmetric unit closely superimpose (RMSD of approximately 0.26 Å) except for the minor loop and N- and C-terminal ends (S6C Fig). The structural zinc is coordinated by side chains of 4 residues (His 24, His 26, His 208, and Asp 293) and a water molecule, in a trigonal bipyramidal geometry [31]. Water bridges His 232 and the resulting O^6 of the purine base, suggesting that both His 293 and the water molecule did play a role in the hydrolysis of the amine. AT-8001 is buried in a closed hydrophobic pocket that can only accommodate a monophosphate compound checked and stabilized by Asn 28, His 74, Ser 106, and Thr 107.

Unlike in the HINT1:AT-8003 complex, there is no ambiguity in substrate nor product binding pose [30]. Once the substrate is bound, the catalytic water attacks the purine C^6, which likely stays at this location while the methylamine is leaving in the opposite exit channel.

Structural and functional analysis of GUK1 specificity

GUK1 is a nucleoside monophosphate kinase able to transfer a phosphate group from ATP to a guanosine 5′-monophosphate, yielding GDP and ADP [25]. Simultaneous binding of monophosphate substrate and triphosphate donor precedes conformational closure and phosphate transfer. This enzyme metabolizes several purine analogues such as abacavir and ganciclovir [32,33]. Expectedly, GUK1 is able to phosphorylate GMP into GDP, but also AT-8001 into AT-8500 (Fig 1B and Table 1). GUK1 is much faster with GMP (control) than with AT-8001 (respectively, 6,800 ± 300 nmol/min/nmol protein versus 34 ± 5 nmol/min/nmol protein). GUK1 exhibits the highest turnover in the activation chain (Table 1), but the 2′-C-methyl, 2′-F modification slows it down approximately 200-fold.

GUK1 was crystallized and its structure solved at 1.76 Å resolution in complex with AT-8001 (Fig 3A and Table 2).

The overall fold of GUK 1 closely resembles that of the yeast and mouse guanylate kinases [34,35]. Two β-sheets and 8 α-helices, the last 2 separated by a π-helix, define 3 structurally and functionally distinct subdomains: the core, the NMP-binding site, and the lid [35]. The core is defined by residues 5 to 31, 97 to 123, and 165 to 194 (helices α1, α4, α7, and α8; strands β1, β7, β8, and β9). The NMP-binding site is a mobile structural element defined by residues 37 to 89 (starting with a protruding loop and followed by helices α2 and α3; strands β3, β4, β5, and β6). The lid where the phosphate donor (e.g., ATP) binds is also mobile and defined by residues 126 to 156 (helices α5 and α6). These parts are interconnected with 4 hinges that allow conformational changes from an open to closed state [34]. The structure presented here is an open conformation (Fig 3A), with the AT-8001 substrate binding through extensive contact with both the phosphate moiety and the nucleobase. Thus, on the one hand, Tyr 81, Tyr 53, and Arg 41 share hydrogen bonding with the oxygen of the phosphate, while Arg 44 makes a contact through a water molecule. On the other hand, Glu 72 and Ser 37 engage hydrogen

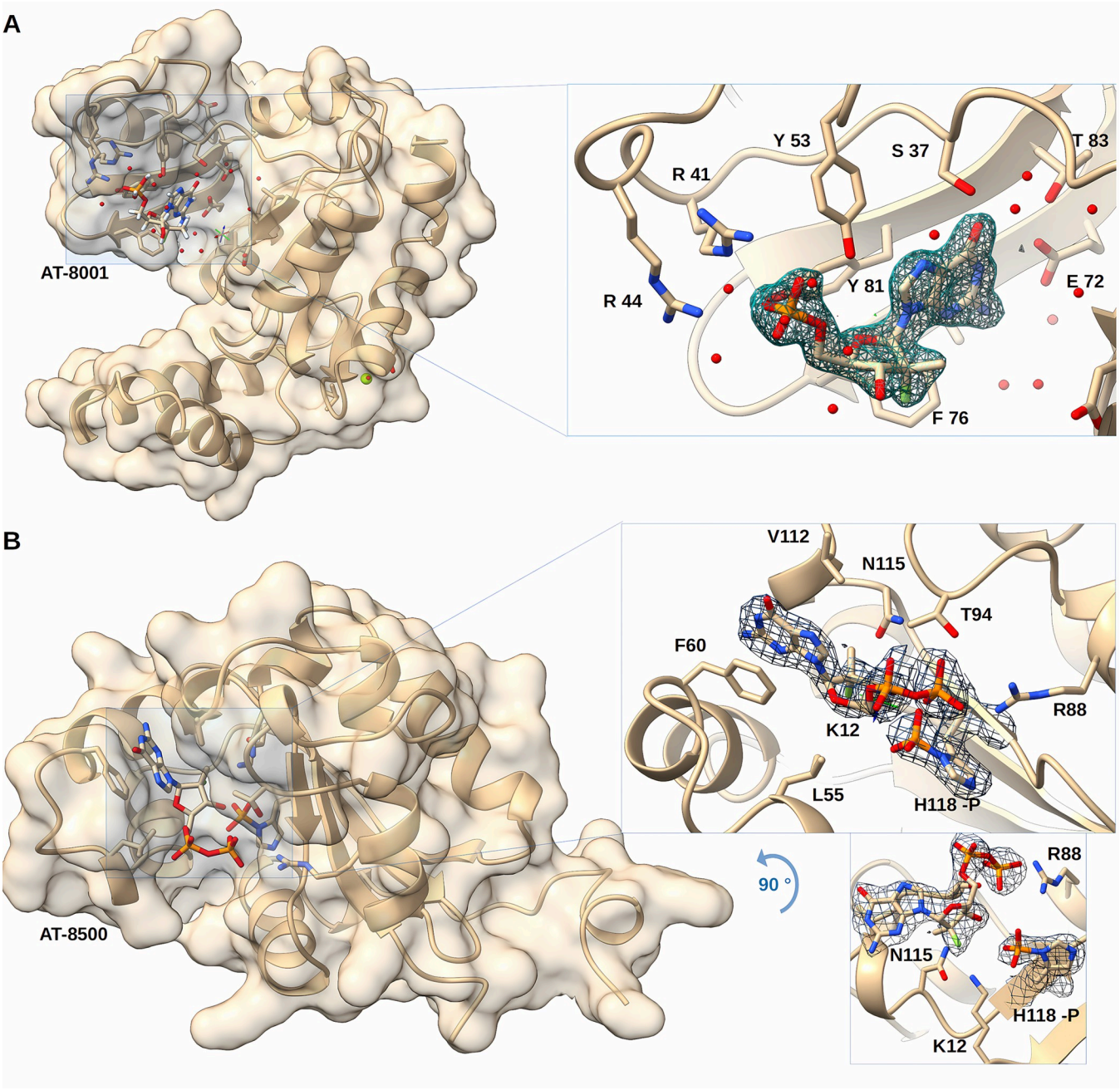

Fig 3. **(A)** Structure of human GUK1 in complex with AT-8001. Human GUK1 structure is represented in ribbon and transparent surface, while compound is represented in sticks with heteroatom colors. The GUK1 structure corresponds to the open conformation, and molecule is binding to the loading site. On the right side, a zoomed part of the molecule is presented in the loading site. Water and side chains of interacting residues with the molecule are shown in sticks. The F_o—F_c omit map of the molecule is presented at 1 σ. **(B)** Structure of human NDPK phosphorylated on H118 and in complex with AT-8500. Human NDPK-B structure (see Materials and methods) is represented in ribbon and transparent surface, while compound is represented in sticks with heteroatom colors. On the right side, a zoomed part of the molecule is presented in the active site in 2 orientations differing by 90˚. Side chains of interacting residues with the molecule are shown in sticks. The F_o—F_c omit map of the molecule as well as the transferred phosphate onto the catalytic histidine is presented at 1 σ. The data underlying this figure can be found at https://doi.org/10.2210/pdb8pts/pdb and https://doi.org/10.2210/pdb8pie/pdb.

https://doi.org/10.1371/journal.pbio.3002743.g003

bonds with the base, while Tyr 53 contributes to positioning the base through π-stacking. The protein structurally checks the substrate by contacting both the purine base and the presence of a monophosphate, with no significant check on the ribose at this stage.

Table 2. Data-collection and refinement statistics for native human enzymes of the bemnifosbuvir activation pathway complexed with substrate or product compounds.

	HINT1 complexed with AT-8003 - 8PWK	ADALP 1 complexed with AT-8001 - 8QCH	GUK 1 complexed with AT-8001 - 8PTS	NDPK complexed with AT-9010 - 8PIE
Wavelength (Å)	0.978	0.980	0.885	0.978
Resolution range	39.80–2.09 2.13–2.09)	105.53–2.44 (2.48–2.44)	62.85–1.76 (1.79–1.76)	49.68–1.90 (1.97–1.90)
Space group	C2	P 21212	C2	P21
Unit cell				
a,b,c	77.9, 46.4, 63.8	142.7, 142.9, 156.4	132.7, 54.3, 58.9	54.2, 120.3, 71.9
α,β,γ	90.0, 94.9, 90.0	90.0, 90.0, 90.0	90.0, 108.8, 90.0	90.0, 110.2, 90.0
Total reflections	89,090	1,216,890	158,084	480,674
Unique reflections	12,964	119,069	37,848	67,263
Multiplicity	6.9 (6.4)	10.2 (10.5)	4.2 (4.3)	7.1 (7.2)
Completeness (%)	95.8 (97)	100 (100)	96.0 (96)	98.9 (98)
Mean I/sigma(I)	10.6 (3.3)	7.2 (1.0)	9.7 (2.2)	11.03 (1.2)
Wilson B-factor	23.3	40.6	27.8	21.5
R-merge	0.11	0.36	0.05	0.24
R-meas	0.12	0.38	0.06	0.25
CC1/2	0.99	0.98	0.99	0.95
No. of reflections used in refinement (free reflections \ 5%)	12,960 (646)	118,763 (5,715)	37,822 (1,823)	67,261 (3,342)
R-work	0.19	0.21	0.24	0.17
R-free	0.23	0.24	0.26	0.21
Total atoms in structure	1,929	23,207	3,232	7,869
Total atoms in macromolecules	1,756	44,365	3,019	7,287
Total atoms in ligands	44	320	80	180
RMS (bonds)	0.007	0.015	0.008	0.030
RMS (angles)	0.09	2.25	1.86	2.28
Ramachandran favored (%)	99.55	97.27	98.4	97.95
allowed (%)	1.06	2.0	1.6	1.4
outliers (%)*	0.0	0.69	0.0	0.68
Average B-factor	48.6	50.0	34.0	26.1
Beamline	Soleil Proxima-1	Soleil Proxima 2	ESRF ID23-1	Soleil Proxima-2

Statistics for the highest-resolution shell are shown in parentheses.

*Outliers are in highly flexible regions of the protein.

https://doi.org/10.1371/journal.pbio.3002743.t002

We modeled AT-8001 into a closed GUK1 conformation based on an energy-minimized model of hGUK1 (S7 Fig). The base is constrained by interactions with Ser 37, Glu 72, and Thr 83. The major difference observed with bound NMP substrates is the ribose pucker conformation. Again, in the structure with bound GMP, the 3'-OH ribose is in *S* pucker position to accommodate the closed conformation of the active site, but not for AT-8001, as described for HINT1 above. To avoid a steric conflict of the 2′-C-methyl, the compound has to slide into the core where the base is π-stacked by Tyr 81 and stabilized by Ser 37 and Glu 72. Both Arg 41 and Arg 44 contact the phosphate; Arg 137 and Arg 148 are expected to catalyze phosphate transfer from ATP bound in the lid, but the repositioning creates distances not compatible for optimal transfer. This positional adjustment likely explains the approximately 200-fold discrimination of AT-8001 versus the natural substrate GMP (Table 1).

Structural and functional basis of NDPK specificity

NDPK is able to transfer a phosphate group from a triphosphate nucleoside donor to a nucleoside diphosphate acceptor [26,36], to yield the active triphosphate form of bemnifosbuvir AT-9010. The reaction proceeds through a so-called "ping-pong" mechanism in which a triphosphate nucleoside transfers covalently its γ-phosphate to the enzyme, and the diphosphate nucleoside acceptor is subsequently bound to the same site to accept the phosphate. NDPK is known to phosphorylate a wide range of NAs bearing various structural modifications. Purified NDPK [27] is able to phosphorylate GDP (control) into GTP and also AT-8500 into AT-9010, the expected product (Fig 1B and Table 1). NDPK shows a high conversion rate and is only 4-fold slower with AT-8500 as substrate than GDP (1,300 ± 100 nmol/min/nmol protein versus 5,400 ± 800, respectively).

We crystallized the NDPK with AT-9010 (Fig 3B).

The crystal structure was solved at 1.9 Å resolution. A hexamer defines the asymmetric unit with 6 extra densities corresponding to 6 AT-8500 diphosphate. Interestingly, only the α and β-phosphates of the 5′-triphosphate moiety are visible. A new density is observed near the NE2 of His 118 of each monomer, which correspond to the histidine phosphorylated state His 118-P in Fig 3B (inset). The AT-9010 γ-phosphate is transferred to the latter due to the protein ability to catalyze the reaction in both directions via a ping-pong mechanism. Structural features of the nucleotide binding site are consistent with the required NDPK substrate promiscuity. Direct comparison with NDPK in complex with GDP (PDB: 1NUE) shows a conserved base-stacking between the guanine and Phe 60. The hydrogen bond between Lys 12 and the 3′-OH of the ribose is no longer present because of a displacement of the ribose, probably due to the 2′-C-methyl, 2′-F modification. This shift allows the 3′-OH to make direct contact with the phosphate group of His 118-P (3 Å). The β-phosphate is engaged in hydrogen bonds with Arg 88 and is facing the catalytic site of the enzyme.

Discussion

Here, we cast light on the activation pathway of bemnifosbuvir and its epimer AT-752. Our work quantitates the differential activation of these substrates relative to their natural counterpart GTP. We visualize and measure essential interactions these 2 compounds and their metabolites engage with specific enzymes involved in their sequential activation.

Turnover measurements (Table 1) show that the rate-limiting steps are generally occurring early in the pathway (CatA/CES1, HINT1, and ADALP1) rather than at the level of the kinases. On these slow, early steps, we note a de-esterification rate approximately 14-fold higher for AT-511 than AT-281 into the common intermediate AT-551 by CatA. Comparatively, CES1 reacts approximately 300-fold slower than CatA with AT-511 but shows an opposite stereopreference with AT-281 being preferred approximately 8-fold over AT-511. These results are aligned with those obtained with PSI-7851, a racemic mixture of PSI-7976 and PSI-7977 (SOF), which shows both the same CatA and stereoisomer preference [14]. A number of NA prodrugs (e.g., SOF, TAF, RDV) need CatA/CES1 [10,11,37,38]-mediated activation. However, CatA is inhibited by the antiviral drug telaprevir (an HCV protease inhibitor) [10,14], an observation that casts light on drug–drug interaction at the molecular level.

Murakami and colleagues [14] have shown that HINT1 is the rate-limiting step along the SOF activation pathway. Its metabolic intermediate PSI-352707 (S1 Fig) binds poorly to HINT1, precluding saturating substrate conditions in infected cells and determination of kcat and Km in enzyme assays. In the case of AT-551, HINT1 is also the rate-limiting step (Table 1). Despite intense crystal soaking efforts using AT-551, we observed only weak positive partial density orthogonal to the expected, "natural substrate" position where phosphate of

AT551 faces the catalytic His 112. Co-crystallization studies resulted in a clean HINT1:AT-8003 complex structure, which proposes a possible structural basis for the kinetic bottleneck along the SOF activation line [14]. It may well be that the higher HINT1 conversion activity of AT-551 as compared to the corresponding intermediate metabolite of SOF, PSI-352707, which differ only by their nucleobase, results from the higher stacking power of purines versus uracil onto Ile 44. The HINT1 limiting step, however, does not seem to impact accumulation of the SOF 5′-triphosphate form (nor AT-9010) in cells. The compound pools are then readily available for selective use by the NS5B viral RdRp in HCV-infected liver cells.

These results indicate that cell types and their relative expression of these "early step" enzymes CatA/CES1 and HINT1 are expected to play a major role in drug activation: (i) the esterase-mediated deprotection step may well govern the overall rate of conversion of the drug into its active metabolite; (ii) the relative abundance of CatA- and CES1-like enzymes should influence these early steps; and (iii) further optimization in antiviral activity might be possible through optimization of the prodrug part in the 5′ portion of the NA rather than focusing on optimizing the kinase steps. The choice of targeted infected cells may ultimately point to the most appropriate epimer and prodrug. In the case of ADALP1, unlike HINT1, the substrate and products are superimposable in the crystal structure, indicating that this complex should be reliable and useful for drug design.

Ideally, the NA activation line must be proven functional in cells, organs, or animal models supporting preclinical tests before commitment to full clinical trials in humans. AlphaFold2 [39]-generated structural models of homologous animal enzymes did not point to obvious polymorphisms potentially deleterious for activation. The very high degree of structural conservation along species suggests a vital role in mammals for these activation enzymes. As such, monitoring differential expression of HINT1 should remain a sufficient and essential asset in predicting P-N hydrolysis in a given tissue or cell. The situation is somewhat similar for ADALP1, which shows significant polymorphisms across organisms, although mapping them invariably points to external, solvent exposed loops, with no direct impact on the NA binding site.

In the case of exposition of cells to bemnifosbuvir, its corresponding 5′-triphosphate AT-9010 has been demonstrated in cellular concentrations up to approximately 700 μM in human primary cells and cell types incubated in vitro with AT-511, including bronchial and nasal epithelial cells [18], hepatocytes, and Huh7 cells [24]. Thus, none of the enzymes studied here limit the formation of the active compound AT-9010 in these cells. Bemnifosbuvir, though, shows reduced antiviral activity in some cell lines, e.g., in VeroE6, HeLa, or MRC-5 cells [18]. We note that *cynomolgus* monkey hepatocytes have been reported to activate bemnifosbuvir to levels 50-fold lower than Huh7 cells [18]. The superimposition of human and *cynomolgus* HINT1 and ADALP1 structures does not point to any polymorphism that could substantiate differences in substrate binding or catalysis.

Bemnifosbuvir shares 2 activation enzymes (HINT1 and NDPK) with SOF and RDV. Hence, the HINT1 structure should represent the most relevant enzyme to optimize the prodrug part of such antivirals. Two other enzymes ADALP1 and GUK1 are specific for diamino purine- and guanine-containing NAs, respectively. With the abacavir success in mind [22], the ADALP1 structure presented here should guide further exploration of chemical diversity at the N^6-amino purine group.

A wealth of structural data already exists regarding NAs in complex with RNA virus replicases, e.g., HCV [15]; picornavirus [40]; Reovirus [41]; SARS-CoV-2 [13,28,42]; for a repository of stacked RdRp structures, see [43]. Much like along the NA activation line, analysis of selectivity of viral polymerase in ternary complexes also identifies proximal amino acid side chains potentially able to accommodate chemical decorations without impacting the NA-5′-triphophate incorporation efficiency.

Finally, an NA drug potential is also conversely determined by its innocuity toward host enzymes that could misuse their 5′-triphosphate form and alter cell metabolism or host nucleic acid. Human mitochondrial RNA polymerase (POLRMT) inhibition accounts, in part, for cellular toxicity of NAs [44]. Much like SOF-TP, AT-9010 is a poor substrate for POLRMT, which uses GTP >69,000-fold better [18]. Comparative examination of ternary complexes of viral RdRps and POLRMT [45] with their RNA and NA-TP substrates may further document the strategy to rationally integrate NA drug design from chemistry to selective inhibition of viral growth [44].

Our work casts light on a whole set of previously ill-defined reactions involved in drug activation and contributes to the integration of NA drug-design from bioavailability to precise and selective mechanism of action as direct-acting antivirals.

Materials and methods

Materials

Recombinant human CatA, cathepsin L (CatL), CES1, and *trans*-epoxy-succinyl-L-leucylamino(4-guanidino)butane (E-64) were purchased from R&D Systems. The respective genes coding for the human recombinant enzymes HINT1, ADALP1, GUK1, and NDPK were coded into a pNC-ET28 expression vector with an N-terminal hexahistidine tag (6xHis) and a TEV protease recognition site, purchased from Twist Bioscience. In humans, the *NDPK* gene is expressed as several isoforms, NDPK-A and NDPK-B being both in synthesis of nucleoside triphosphates other than ATP. The sequence of NDPK-B [26,27,46] was used throughout the study. Control compound AMP-NH_2 was from Biosynth, N^6-Me-AMP was purchased from BioLog Life Science Institute, and AMP, IMP, GMP, GDP, and GTP were from Sigma Aldrich. Other compounds with a name starting with "AT" were synthesized by TopPharm, USA.

Protein expression

The DNA sequence encoding for ADALP1, NDPK, GUK1, and HINT1 were synthesized and cloned into a pET-28a (+) vector for HINT1 and GUK1, into a pNC-ET28 vector for NDPK, and into a pET-28 for ADALP1 (Twist Biosciences).

All proteins were expressed in *E. coli* NEB C2566 cells (New England Biolabs). The cells were grown at 37˚C in TB medium for HINT1, GUK1, and NDPK and LB Broth for ADALP1 containing 50 μg/mL Kanamycin until the absorbance at 600 nm reached 0.6 to 0.8. At this stage, induction was started with 0.5 mM IPTG and the cells were grown overnight at 16˚C. Then, the cells were harvested and the pellets were suspended in lysis buffer (50 mM Tris (pH = 8.0), 300 mM NaCl, 10 mM imidazole, 1 mM PMSF, 0.25 mg/mL lysozyme, and 10 μg/mL DNase) for HINT1, GUK1, and NDPK, before storing them at −80˚C. For ADALP1, the pellet was freeze-dried and stored at −80˚C.

HINT1, GUK1, and NDPK purification

The lysate was disrupted and cleared by centrifugation at 12,000*g* for 30 min at 10˚C. Then, the supernatant was loaded onto a Ni-NTA-beads (Thermo Fisher) batch and washed with 50 mM Tris (pH = 8.0), 300 mM NaCl, 20 mM imidazole buffer. The recombinant protein was then eluted with 50 mM Tris (pH = 8.0), 300 mM NaCl, 250 mM imidazole buffer. About 10% glycerol was added for HINT1. TEV protease was used to remove the N-terminus His-tag during an overnight dialysis in a buffer (50 mM Tris (pH = 8.0), 150 mM NaCl, 1 mM DTT) at 4˚C for HINT1, at 37˚C for GUK1, and at room temperature for NDPK.

A second purification step on Ni-NTA beads was performed to remove any uncleaved protein before to achieve a SEC purification onto a Superdex 75 16/600 GE column (GE Healthcare) in a final buffer containing 10 mM Tris (pH = 8.0), 50 mM NaCl for HINT1; 20 mM Tris (pH = 8.0), 100 mM NaCl, 1 mM DTT for GUK1; and 50 mM Tris (pH = 8.0), 150 mM NaCl, 1 mM DTT for NDPK. The fractions were analyzed on SDS-PAGE and the ones containing the pure target protein were pooled. The purified protein was then concentrated until 10 mg/mL, aliquoted, and stored at −80˚C. Same protocol was used to express and purify uncleaved NDPK for activity assays.

ADALP1 purification

Bacterial pellets were lysed in half buffer (50 mM HEPES (pH = 7.5), 300 mM NaCl, 10% glycerol, 0.5 mM TCEP) and half Master Mix Bug Buster (Merck) supplemented with a tablet of EDTA-free antiprotease cocktail (Roche) per 50 ml of lysate before sonication.

The lysate was cleared by centrifugation at 12,000*g* for 30 min at 10˚C, and the supernatant was applied onto a Talon Superflow beads batch (Merck). The immobilized proteins were washed with 50 mM HEPES (pH 7.5), 300 mM NaCl, 12.5 mM imidazole, 10% glycerol, 0.5 mM TCEP, then washed with 50 mM HEPES (pH 7.5), 1.5M NaCl, 10% glycerol, 0.5 mM TCEP, and eluted in buffer (50 mM HEPES (pH 7.5), 300 mM NaCl, 150 mM imidazole, 10% glycerol, 0.5 mM TCEP).

TEV protease was used to remove the N-terminus His-tag during an overnight dialysis in a buffer 50 mM HEPES (pH = 7.5), 300 mM NaCl, 10% glycerol, 1 mM DTT. The untagged ADALP1 was further purified by a Talon Superflow beads batch (Merck).

Finally, ADALP1 was purified by size exclusion chromatography using a S75 16/60 GE Column (GE Healthcare) equilibrated in buffer containing 10 mM Tris (pH = 8.0), 40 mM NaCl, 1 mM TCEP. The single ADALP1 peak corresponded to the monomeric form. It was concentrated to 10 mg/mL, flash-frozen in liquid nitrogen, and stored at −80˚C.

CatA enzyme assay

Human recombinant CatA was first activated by following the manufacturer's instructions (R&D Systems), incubating at 37˚C 10 μg/mL CatA with 1 μg/mL CatL in an activation buffer (25 mM MES (pH = 6.0), 5 mM DTT) during 30 min. About 10 μM E-64 (CatL inhibitor) was then added before aliquoting and storage of activated CatA at −80˚C. AT-511 and AT-281 hydrolysis by activated CatA was measured by incubating 100 μM compound in a reaction buffer containing 25 mM MES (pH 6.5), 100 mM NaCl, 1 mM DTT, 0.1% NP-40, and 20 nM enzyme at 37˚C for 45 min. The reaction was started by adding the enzyme. At various time points, 10 μL aliquots were collected from the reaction mixtures mixed with EDTA 10 mM (final concentration) and stopped by heating the samples at 95˚C for 5 min. The sample were filtered on centrifugal filters Microcon—10 (Sigma Aldrich). The filtrates were mixed with triethylammonium bicarbonate (TEAB) 1M (1:1) and analyzed onto a C18 reverse phase column (2.5 μm, 4.6 by 100 mm, Xbridge C18 BEH, Waters) equipped with a guard column; substrates and products were detected at 260 nm and eluted at a flow rate of 1 ml/min at 35˚C with a gradient of 0% to 4% of MeCN in TEAB 50 mM (pH = 7) in 10 min.

CES1 enzyme assay

AT-511 and AT-281 hydrolysis by human recombinant CES1 (100 nM) was assayed by incubating at 37˚C the enzyme with 100 μM compound in 50 mM Tris buffer (pH = 7.5), 0.1% NP-40 and 1 mM DTT for 2 h. The reaction was started by adding the substrate. At various time points, 20 μL aliquots were collected from the reaction mixtures mixed with EDTA 10 mM

(final concentration) and stopped by heating the samples at 95˚C for 5 min. The sample were filtered on centrifugal filters Microcon—10 (Sigma–Aldrich). The filtrates were mixed with TEAB 1M (1:1) and analyzed onto a C18 reverse phase column (2.5 μm, 4.6 by 100 mm, Xbridge C18 BEH, Waters) equipped with a guard column; substrates and products were detected at 260 nm and eluted at a flow rate of 1 ml/min at 35˚C with a gradient of 0% to 4% of MeCN in TEAB 50 mM (pH = 7) in 10 min.

HINT1 enzyme assay

The hydrolytic reactions with HINT1 (100 nM) were performed on AMP-NH_2 and AT-551 (200 μM) in 20 mM HEPES buffer (pH 7.2), 20 mM KCl, 1 mM $MgCl_2$, and 1 mM DTT, at 37˚C for 2 h. The reaction was started by adding the enzyme. At various time points, 10 μL aliquots were collected from the reaction mixtures mixed with EDTA 10 mM (final concentration) and stopped by heating the samples at 95˚C for 5 min. The sample are filtered on AcroPrep Advance 96-Well Filter Plates with 3K Omega membrane (Pall). The filtrates were mixed with TEAB 1M and analyzed onto a C18 reverse phase column (3 μm, 3 by 150 mm, Acclaim Polar Advantage II, Thermo Fisher) equipped with a guard column; substrates and products were detected at 260 nm and eluted at a flow rate of 0.5 ml/min at 30˚C with a gradient of 0% to 15% of MeCN in TEAB 50 mM (pH = 7) in 17 min.

ADALP1 enzyme assay

ADALP1 (100 nM) activity was measured on several substrates (N^6-Me-AMP, AT-8003, AT-8002, AT-8004, AT-8010, AT-551, AT-259, AT-229) at 200 μM concentration in a reaction buffer containing BTP (pH = 6.8), 100 mM NaCl, and 1 mM DTT. Reactions were incubated at 37˚C for 2 h. About 1 μM ADALP1 was also tested with AT-8002, AT-551, AT-229, and AT-259. The reaction was started by adding the substrate. At various time points, 10 μL aliquots were collected from the reaction mixtures diluted with H_2O and stopped by heating the samples at 95˚C for 5 min. The sample were filtered on AcroPrep Advance 96-Well Filter Plates with 3K Omega membrane (Pall). The filtrates were mixed with TEAB 1M and analyzed onto a C18 reverse phase column (2.5 μm, 4.6 by 100 mm, Xbridge C18 BEH Premier, Waters) equipped with a guard column; N^6-Me-AMP, AT-8002, and products were detected at 260 nm and eluted at a flow rate of 1 ml/min at 35˚C with a gradient of 0% to 10% of MeCN in TEAB 50 mM (pH = 7) in 10 min. AT-8003, AT-551, and products were eluted at a flow rate of 1 ml/min at 35˚C with a gradient of 0% to 15% of MeCN in TEAB 50 mM (pH = 7) in 10 min. AT-8004, AT-8010, AT-229, AT-259, and products were eluted at a flow rate of 1 ml/min at 35˚C with a gradient of 0% to 25% of MeCN in TEAB 50 mM (pH = 7) in 10 min.

GUK1 enzyme assay

GUK1 (40 nM) was assayed on GMP, AT-8003, and AT-8001 (200 μM) in a reaction buffer containing 50 mM Tris buffer (pH = 8.0), 50 mM KCl, 5 mM $MgCl_2$, 1 mM ATP, and 1 mM DTT. Reactions were incubated at 37˚C for 1 h. The reaction was started by adding the enzyme. At various time points, 10 μL aliquots were collected from the reaction mixtures, mixed with EDTA 10 mM (final concentration), and stopped by heating the samples at 95˚C for 5 min. The sample were filtered on AcroPrep Advance 96-Well Filter Plates with 3K Omega membrane (Pall). The filtrates were mixed with TEAB 1M and analyzed onto a C18 reverse phase column (3 μm, 3 by 150 mm, Acclaim Polar Advantage II, Thermo Fisher) equipped with a guard column and equilibrated with TEAB 50 mM (pH = 7) (buffer A). Substrates and products were detected at 260 nm and eluted at a flow rate of 0.5 ml/min at 30˚C with a gradient of 0% to 10% of MeCN in TEAB 50 mM (pH = 7) in 12 min.

NDPK enzyme assay

NDPK (20 nM) was assayed on GDP and AT-8500 (200 μM) in a reaction buffer containing 50 mM Tris buffer (pH = 8.0), 50 mM KCl, 5 mM $MgCl_2$, 1 mM ATP, and 1 mM DTT. Reactions were incubated at 37˚C for 1 h. The reaction was started by adding the enzyme. At various time points, 10 μL aliquots were collected from the reaction mixtures mixed with EDTA 10 mM and stopped by heating the samples at 95˚C for 5 min. The samples were filtered on Acro-Prep Advance 96-Well Filter Plates with 3K Omega membrane (Pall). The filtrates were mixed with TEAB 1M and analyzed onto a C18 reverse phase column (3 μm, 3 by 150 mm, Acclaim Polar Advantage II, Thermo Fisher) equipped with a guard column; substrates and products were detected at 260 nm and eluted at a flow rate of 0.5 ml/min at 30˚C with a gradient of 0% to 10% of MeCN in TEAB 50 mM (pH = 7) in 12 min.

Crystallization of HINT1

Crystallization conditions were adapted from [21]. Briefly, co-crystals with AT-8003 were grown at 293.15 K, using a 1:1 ratio of HINT1 at 10 mg/mL with AT-8003 (final concentration 25 mM) to precipitant solution 0.1 M MES (pH 6.1 to 6.5), 27% to 30% PEG 8000. Crystals grew in a few days and were cryo-protected with reservoir solution supplemented with 20% PEG 400, and flash-frozen in liquid nitrogen at 100 K.

Crystallization of ADALP1

Crystallization assay were set up using the sitting drop vapor diffusion method, using a 2:1 ratio of protein solution to the reservoir solution at 293.15 K. The co-crystals with AT-8001 were obtained by mixing ADALP1 at 17 mg/mL with AT-8003 (final concentration 10 mM) and 1:10,000 w/w dilution a-Chymotrypsin prior to crystallization and were grown from 1.1 to 2.1 M ammonium sulfate, 0.1 M sodium cacodylate/HCl (pH 5.3 to 6.3), and 0.2 M sodium chloride for 2 mo. Crystals were cryo-protected with reservoir solution supplemented with 20% glycerol and flash-frozen in liquid nitrogen at 100 K.

Crystallization of GUK1

Large co-crystals of GUK1 (17 mg/mL) with AT-8001 (2 mM) supplemented with 5 mM MgCl2 were grown using the sitting drop method with a 3:1 ratio of protein solution to precipitant solution consisting of 66 mM sodium cacodylate (pH 6.5 to 7.5), 12.2% to 22.2% PEG 3350, 8.3% PEG 4000, 33 mM MES (pH 6.5), and 66 mM magnesium chloride over a period of 10 d at 293.15 K. Crystals were cryo-protected with reservoir solution supplemented with 20% glycerol and flash-frozen in liquid nitrogen at 100 K.

Crystallization of NDPK

Crystallization conditions were adapted from [46] using the sitting-drop vapor diffusion method using crystallization buffer. All crystals were grown at 277.15 K, using a 1:1 ratio of protein (5 mg/mL) mixed with AT-9010 (final concentration 1 mM) to precipitant solution (12% PEG 4000, 50 mM Tris (pH = 8.4), 16% glycerol, 1 mM DTT). Crystals grew in 3 d and were flash-frozen directly in liquid nitrogen at 100 K.

Structure determination of the human HINT1:AT-8003 complex

The dataset of HINT1 in complex with AT-8003 was collected on the Proxima-1 beamline at the Synchrotron SOLEIL. Dataset was processed using AUTOPROC [47]. The phase was obtained using Molecular Replacement using MOLREP [48] with the PDB entry 6N3V as a

model. The ligand AT-8003 and geometry description files were generated using the GRADE2 server [49]. Structure handling and refinement were done using COOT [50] and BUSTER [51].

Structure determination of the human ADALP 1:AT-8001 complex

The dataset of ADALP 1 in complex with AT-8001 was collected on the Proxima-2 beamline at the Synchrotron SOLEIL. Dataset was processed using AUTOPROC [47], and processed data were sent to the CCP4 cloud suite [52]. The pipeline is fully automatic. The phase was obtained using Molecular Replacement–MORDA [52] using PDB entry 6IV5 as a model. The ligand AT-8001 and geometry description files were generated using the GRADE2 server [49]. Minor correction on the structure and further refinement were done using COOT [50] and REFMAC5 [53], respectively.

Structure determination of the human GUK 1:AT-8001 complex

The dataset of GUK1 in complex with AT-8001 was collected on the ESRF ID23-1 beamline. Dataset was processed using AUTOPROC [47]. The phase was obtained using Molecular Replacement–MORDA [52] using PDB entry 4F4J as a search model and optimized with ARP/WARP [54]. Structure refinement was done using COOT [50] and BUSTER [51], respectively.

Structure determination of the human NDPK:AT-8500 complex

The dataset of NDPK in complex with AT-8500 was collected on the Proxima-2 beamline at the Synchrotron SOLEIL. Dataset was handled using the CCP4 suite [55]. Images were processed by XDS [56] and AIMLESS [57]. The phase was obtained using Molecular Replacement–PHASER [58] with the PDB entry 1NUE as a model. The ligand AT-8500 corresponding to the diphosphate form of AT-9010 was generated using the AceDRG program [59]. Structure handling and refinement were done using COOT [50] and REFMAC5 [53] software, respectively.

All electron-density maps were inspected using COOT [50]. Extra density accounting for ions, and/or compounds were observed for all complexed structures. The structures were evaluated using MOLPROBITY [60] and PROCHECK [61]. Structural analysis and high-resolution figures were done with UCSF ChimeraX [62]. Facilities, statistics of data collections, refinements, and PDB deposition code are given in Table 2.

Modeling of GUK 1 closed conformation

Sequence of human GUK 1 was submitted to an homology modeling process using modeler V10 and the structure of mouse GUK complexed with GMP and ADP (PDB 1LVG) as template. The 2 sequences have 88% identity, which makes us confident that the resulting closed conformation model is reasonable.

Docking of AT-8003 onto HINT1

The 3D model of HINT1 was energy minimized by the steepest gradient method of energy minimization followed by conjugate gradient minimization, using the MMTK and AMBER-packages [63–65]. Mol2 and PDB files format of the ligands and receptor were converted to PDBQT format using CHIMERA prior to docking. All the water and solvent atoms of the protein were removed, and the polar hydrogen and polar charge were added onto the ions and ligand prior to docking. The protein was kept rigid, while the ligand was allowed to rotate and

explore more flexible binding pockets. Docking of the respective ligands into the cavity were performed iteratively using AUTODOCK VINA—version 1.1.2 [66]. The best poses from the first round of docking were used as seed for the second round. The resulting first round of docking were carefully analyzed to retain the best poses. The grid box size dimensions was designed to include the long binding cleft and the catalytic site; its dimensions were 37.87 × 16.12 × 20.89. The default scoring function was used for docking.

Ten binding modes of the docked complexes were obtained and sorted based on their binding energy, and amino acid residues present at a distance less of 3 Å were considered as the binding partners of the ligands. Six binding modes with the phosphate oriented toward the catalytic site were kept and compared to the experimental structure. One binding mode is overlapped with the structure. A control experiment with AMP was also performed. Figures representing the docked complexes have been generated using CHIMERA [62].

Docking of GMP and AT-8001 in GUK1 closed conformation

The 3D model of GUK 1 was energy minimized by the steepest gradient method of energy minimization followed by conjugate gradient minimization, using the MMTK and AMBER packages [63–65]. Mol2 and PDB files format of the ligands and receptor were converted to PDBQT format using chimera prior to docking. All the water and solvent atoms of the protein were removed, and the polar hydrogen and polar charge were added onto the ions and ligand prior to docking. The protein was kept rigid, while the ligand was allowed to rotate and explore more flexible binding pockets. Docking of the respective ligands into the cavity were performed iteratively using AUTODOCK VINA [66]. The best poses from the first round of docking were used as seed for the second round. The resulting first round of docking were carefully analyzed to retain the best poses. The grid box size dimensions were first 40 × 40 × 40, to verify that our ligands will preferentially bind in the catalytic site. The grid box size was further optimized to 23.2 × 25.6 × 21.2, thus covering the binding pockets; the default scoring function was used for docking. As control for the procedure, GMP was docked following the same protocol, and the final pose is virtually identical to the one measure in the experimental structure (PDB 1LVG).

Binding modes of the docked complexes were obtained and sorted based on their binding energy; ions and amino acid residues present at a distance less of 3 Å were considered as the binding partners of the ligands. Binding modes were compared to theses of the native structure. The interaction figures representing the docked complexes have been generated using CHIMERAX [67].

Supporting information

S1 Fig. Structure of NAs other than-AT-compounds. (A) RDV or GS-5734, aryloxy phophoramidate prodrug of an adenosine analogue, with 1′-C-nucleoside bond and 1′-cyano substitution. (B) TAF or GS-7340, prodrug of tenofovir, acyclic phosphonate analogue of adenosine monophosphate. (C) GS-6620, aryloxy phosphoramidate prodrug of an adenosine analogue, with 1′-C-nucleoside bond and 1′-cyano-2′-C-methyl substitutions. (D) SOF or PSI-7977 (S_P diastereoisomer) and related compounds PSI-7976 (R_P diastereoisomer) and PSI-7851 (mixture of both diastereoisomers), aryloxy phosphoramidate prodrug of uridine analogue with a 2′-fluoro-2′ -C-methyl modified ribose. (E) PSI-352707, phosphoramidate metabolite of SOF. NA, nucleoside/nucleotide analogue; RDV, remdesivir; SOF, sofosbuvir; TAF, tenofovir alafenamide.
(TIFF)

S2 Fig. Gels SDS-PAGE of purified enzymes HINT1, ADALP1, GUK1, and NDPK. Key: Lysate (Lys), Flow-through (FT), Wash (W), Eluate (E), Tag cleavage eluate (Cleavage), Gel filtration (GF). The data underlying this supporting figure can be found at https://zenodo.org/records/12606239. ADALP1, adenosine deaminase-like protein 1; GUK1, guanylate kinase 1; HINT1, histidine triad nucleotide 1; NDPK, nucleoside diphosphate kinase.
(TIF)

S3 Fig. Structure of (**A**) AT-compounds and (**B**) reference compounds mentioned in the manuscript.
(TIF)

S4 Fig. CatA/CES1 stereoselectivity. Activity of CatA (panel A) or CES1 (panel B) with either AT-511 (S_P isomer) or AT-281 (R_P isomer) as substrates. Approximately 20 nM CatA was incubated 45 min at 37˚C with 100 μM substrate. About 100 nM CES1 was incubated 2 h at 37˚C with 100 μM substrate. Bars show mean values (± SD) of 3 independent experiments. The data underlying this supporting figure can be found at https://zenodo.org/records/12606239.
(TIF)

S5 Fig. Specificity and order of the reactions. Activation pathway of bemnifosbuvir follows this specific order of reaction. As shown in Table 1, activity assay of ADALP1 with AT-551 as substrate and GUK1 with AT-8003 as substrate did not show any conversion even with 10-fold more enzyme than our standard protocol.
(TIF)

S6 Fig. Human ADALP1 structure analysis. (A) The protein structure is represented in cylinders and stubs and colors in rainbow color code. Different orientations are presented in respect to the previous one. **(B)** Multiple Angle Light Scattering result graph, presenting the elution curve followed at 280 nm (blue line) and the corresponding scattering graph (orange line), experiment show the homogenity of the sample. **(C)** The asymmetric unit contained 8 molecules that all contained the compound, presented the superimposition of the 8 chains present showing that they are virtually identical.
(TIF)

S7 Fig. A model of human GUK1 in its closed conformation. The human GUK1 model is represented in ribbon and transparent surface, while the compound is represented in sticks with heteroatom colors and ADP (brown) at the active site. In the left panel is presented GUK1 in complex with GMP (yellow); in the central and right panel are presented, respectively, GUK1 in complex with AT-8001 in its theoretical position (blue), i.e., superposed with GMP and docked (pink) in the cavity. Below is presented a comparison of the superimposition of the GMP with the theoretical position of AT-8001, highlighting a different ribose pucker conformation, and the superimposition of the theoretical position of AT-8001 with the docked AT-8001, highlighting a tilting of the ribose and the base to reduce steric hindrance between the 2′ methyl with the main chain.
(TIF)

S8 Fig. Ligand binding to HINT1 determined using ITC. (A) Titration of AMP binding onto HINT1. Top part of the figure shows an exothermic association of AMP and HINT1; bottom part shows the fitting of the data considering 1 site model association, showing *K*a approximately 1.7 10^4 M^{-1}. **(B)** Titration of AT-8003 binding onto HINT1. The experimental condition fails to report association. Top part of the figure shows absence of peaks defining association of AT-8003 to HINT1; bottom part shows the random fitting of the data

considering 1 site model. The data underlying this supporting figure can be found at https://zenodo.org/records/12606239.
(TIF)

S9 Fig. Docking studies of ligands onto HINT1. (A, B) Two views (side and tilted) visualizing the criteria for docking experiment: HINT1 structure is presented as the accessible surface (colored wheat). The green box represents the docking grid encompassing the binding and catalytic site; AT-8003 in predocking position (colored in blue) is outside the computational grid and far from the protein target. **(C)** Docking result overlapping all 10 poses. Docked molecules are colored in light green. None of the molecules are binding following the binding cleft. **(D)** Similar to C except only remains the 6 poses for which the phosphate is oriented toward the catalytic site. **(E)** The one pose that is similar to the experimental data. **(F, G, H)** Superimposition of the docked AT-8003 with the AT-8003 (colored in light pink) measured by crystallography. Phosphate, ribose, and part of the base are fully superimposed, and only the extremity of the base is shifted. **(I)** Control of docked AMP (colored in purple) showing that the molecule is fully positioned within the binding site.
(TIF)

S1 Raw Images. Raw blots for S2 Fig.
(PDF)

Acknowledgments

We thank Veronique Fattorini, Camille Falcou, and Pierre Gauffre for synthetic gene design and help in protein purification. We thank Nancy Agrawal, Alex Vo, and Qi Huang for critical reading of the manuscript, together with Ashleigh Shannon and numerous colleagues for helpful suggestions along the project.

The authors acknowledge La Fondation CNRS for funding management, SOLEIL and ESRF for provision of synchrotron radiation facilities, and we would like to thank beamline teams of Proxima-1, Proxima-2 and ID23-eh1 for their assistance during data collection.

Author Contributions

Conceptualization: Karine Alvarez, François Ferron, Bruno Canard.

Data curation: François Ferron.

Formal analysis: Aurélie Chazot, Claire Zimberger, Mikael Feracci, Adel Moussa, Steven Good, Karine Alvarez, François Ferron, Bruno Canard.

Funding acquisition: Karine Alvarez, Bruno Canard.

Investigation: Aurélie Chazot, Claire Zimberger, Mikael Feracci, Adel Moussa, Karine Alvarez, François Ferron.

Methodology: Steven Good, Karine Alvarez, François Ferron, Bruno Canard.

Project administration: Jean-Pierre Sommadossi, Bruno Canard.

Supervision: Jean-Pierre Sommadossi, François Ferron, Bruno Canard.

Writing – original draft: François Ferron, Bruno Canard.

Writing – review & editing: Karine Alvarez, François Ferron, Bruno Canard.

References

1. Adamson CS, Chibale K, Goss RJM, Jaspars M, Newman DJ, Dorrington RA. Antiviral drug discovery: preparing for the next pandemic. Chem Soc Rev. 2021; 50:3647–3655. https://doi.org/10.1039/d0cs01118e PMID: 33524090
2. Seley-Radtke KL, Yates MK. The evolution of nucleoside analogue antivirals: A review for chemists and non-chemists. Part 1: Early structural modifications to the nucleoside scaffold. Antiviral Res. 2018; 154:66–86. https://doi.org/10.1016/j.antiviral.2018.04.004 PMID: 29649496
3. Yates MK, Seley-Radtke KL. The evolution of antiviral nucleoside analogues: A review for chemists and non-chemists. Part II: Complex modifications to the nucleoside scaffold. Antiviral Res. 2019; 162:5–21. https://doi.org/10.1016/j.antiviral.2018.11.016 PMID: 30529089
4. Geraghty RJ, Aliota MT, Bonnac LF. Broad-Spectrum Antiviral Strategies and Nucleoside Analogues. Viruses. 2021; 13:667. https://doi.org/10.3390/v13040667 PMID: 33924302
5. Slusarczyk M, Serpi M, Pertusati F. Phosphoramidates and phosphonamidates (ProTides) with antiviral activity. Antivir Chem Chemother. 2018; 26:2040206618775243. https://doi.org/10.1177/2040206618775243 PMID: 29792071
6. Mehellou Y, Rattan HS, Balzarini J. The ProTide Prodrug Technology: From the Concept to the Clinic: Miniperspective. J Med Chem. 2018; 61:2211–2226. https://doi.org/10.1021/acs.jmedchem.7b00734 PMID: 28792763
7. Mackman RL. Phosphoramidate Prodrugs Continue to Deliver, The Journey of Remdesivir (GS-5734) from RSV to SARS-CoV-2. ACS Med Chem Lett. 2022; 13:338–347. https://doi.org/10.1021/acsmedchemlett.1c00624 PMID: 35291757
8. Shannon A, Canard B. Kill or corrupt: Mechanisms of action and drug-resistance of nucleotide analogues against SARS-CoV-2. Antiviral Res. 2023; 210:105501. https://doi.org/10.1016/j.antiviral.2022.105501 PMID: 36567022
9. Johnson KA, Dangerfield T. Mechanisms of inhibition of viral RNA replication by nucleotide analogs. Enzymes. 2021; 49:39–62. https://doi.org/10.1016/bs.enz.2021.07.001 PMID: 34696838
10. Li R, Liclican A, Xu Y, Pitts J, Niu C, Zhang J, et al. Key Metabolic Enzymes Involved in Remdesivir Activation in Human Lung Cells. Antimicrob Agents Chemother. 2021; 65:e0060221. https://doi.org/10.1128/AAC.00602-21 PMID: 34125594
11. Li J, Liu S, Shi J, Zhu H-J. Activation of Tenofovir Alafenamide and Sofosbuvir in the Human Lung and Its Implications in the Development of Nucleoside/Nucleotide Prodrugs for Treating SARS-CoV-2 Pulmonary Infection. Pharmaceutics. 2021; 13:1656. https://doi.org/10.3390/pharmaceutics13101656 PMID: 34683949
12. Wang Q, Wu J, Wang H, Gao Y, Liu Q, Mu A, et al. Structural Basis for RNA Replication by the SARS-CoV-2 Polymerase. Cell. 2020; 182:417–428.e13. https://doi.org/10.1016/j.cell.2020.05.034 PMID: 32526208
13. Kokic G, Hillen HS, Tegunov D, Dienemann C, Seitz F, Schmitzova J, et al. Mechanism of SARS-CoV-2 polymerase stalling by remdesivir. Nat Commun. 2021; 12:279. https://doi.org/10.1038/s41467-020-20542-0 PMID: 33436624
14. Murakami E, Tolstykh T, Bao H, Niu C, Steuer HMM, Bao D, et al. Mechanism of activation of PSI-7851 and its diastereoisomer PSI-7977. J Biol Chem. 2010; 285:34337–34347. https://doi.org/10.1074/jbc.M110.161802 PMID: 20801890
15. Appleby TC, Perry JK, Murakami E, Barauskas O, Feng J, Cho A, et al. Viral replication. Structural basis for RNA replication by the hepatitis C virus polymerase. Science. 2015; 347:771–775. https://doi.org/10.1126/science.1259210 PMID: 25678663
16. Toussi SS, Hammond JL, Gerstenberger BS, Anderson AS. Therapeutics for COVID-19. Nat Microbiol. 2023; 8:771–786. https://doi.org/10.1038/s41564-023-01356-4 PMID: 37142688
17. Horga A, Saenz R, Yilmaz G, Simón-Campos A, Pietropaolo K, Stubbings WJ, et al. Oral bemnifosbuvir (AT-527) vs placebo in patients with mild-to-moderate COVID-19 in an outpatient setting (MORNINGSKY). Future Virol. 2023. https://doi.org/10.2217/fvl-2023-0115 PMID: 37928891
18. Good SS, Moussa A, Zhou X-J, Pietropaolo K, Sommadossi J-P. Preclinical evaluation of AT-527, a novel guanosine nucleotide prodrug with potent, pan-genotypic activity against hepatitis C virus. PLoS ONE. 2020; 15:e0227104. https://doi.org/10.1371/journal.pone.0227104 PMID: 31914458
19. Good SS, Shannon A, Lin K, Moussa A, Julander JG, La Colla P, et al. Evaluation of AT-752, a Double Prodrug of a Guanosine Nucleotide Analog with In Vitro and In Vivo Activity against Dengue and Other Flaviviruses. Antimicrob Agents Chemother. 2021; 65:e0098821. https://doi.org/10.1128/AAC.00988-21 PMID: 34424050

20. Feracci M, Eydoux C, Fattorini V, Lo Bello L, Gauffre P, Selisko B, et al. AT-752 targets multiple sites and activities on the Dengue virus replication enzyme NS5. Antiviral Res. 2023; 212:105574. https://doi.org/10.1016/j.antiviral.2023.105574 PMID: 36905944

21. Shah R, Maize KM, Zhou X, Finzel BC, Wagner CR. Caught before Released: Structural Mapping of the Reaction Trajectory for the Sofosbuvir Activating Enzyme, Human Histidine Triad Nucleotide Binding Protein 1 (hHint1). Biochemistry. 2017; 56:3559–3570. https://doi.org/10.1021/acs.biochem.7b00148 PMID: 28691797

22. Schinkmanová M, Votruba I, Shibata R, Han B, Liu X, Cihlar T, et al. Human N6-Methyl-AMP/DAMP Aminohydrolase (Abacavir 5'-Monophosphate Deaminase) is Capable of Metabolizing N6-Substituted Purine Acyclic Nucleoside Phosphonates. Collect Czech Chem Commun. 2008; 73:275–291. https://doi.org/10.1135/cccc20080275

23. Murakami E, Bao H, Mosley RT, Du J, Sofia MJ, Furman PA. Adenosine Deaminase-like Protein 1 (ADAL1): Characterization and Substrate Specificity in the Hydrolysis of N 6—or O 6 -Substituted Purine or 2-Aminopurine Nucleoside Monophosphates. J Med Chem. 2011; 54:5902–5914. https://doi.org/10.1021/jm200650j PMID: 21755941

24. Good SS, Westover J, Jung KH, Zhou X-J, Moussa A, La Colla P, et al. AT-527, a double prodrug of a guanosine nucleotide analog, is a potent inhibitor of SARS-CoV-2 in vitro and a promising oral antiviral for treatment of COVID-19. Antimicrob Agents Chemother. 2021. https://doi.org/10.1128/AAC.02479-20 PMID: 33558299

25. Khan N, Shah PP, Ban D, Trigo-Mouriño P, Carneiro MG, DeLeeuw L, et al. Solution structure and functional investigation of human guanylate kinase reveals allosteric networking and a crucial role for the enzyme in cancer. J Biol Chem. 2019; 294:11920–11933. https://doi.org/10.1074/jbc.RA119.009251 PMID: 31201273

26. Georgescauld F, Song Y, Dautant A. Structure, Folding and Stability of Nucleoside Diphosphate Kinases. Int J Mol Sci. 2020; 21:6779. https://doi.org/10.3390/ijms21186779 PMID: 32947863

27. Attwood PV, Muimo R. The actions of NME1/NDPK-A and NME2/NDPK-B as protein kinases. Lab Invest. 2018; 98:283–290. https://doi.org/10.1038/labinvest.2017.125 PMID: 29200201

28. Shannon A, Fattorini V, Sama B, Selisko B, Feracci M, Falcou C, et al. A dual mechanism of action of AT-527 against SARS-CoV-2 polymerase. Nat Commun. 2022; 13:621. https://doi.org/10.1038/s41467-022-28113-1 PMID: 35110538

29. Jia Q, Xie W. Alternative conformation induced by substrate binding for Arabidopsis thalianaN6-methyl-AMP deaminase. Nucleic Acids Res. 2019; 47:3233–3243. https://doi.org/10.1093/nar/gkz070 PMID: 30721978

30. Romero-Romero S, Kordes S, Michel F, Höcker B. Evolution, folding, and design of TIM barrels and related proteins. Curr Opin Struct Biol. 2021; 68:94–104. https://doi.org/10.1016/j.sbi.2020.12.007 PMID: 33453500

31. Zheng H, Chordia MD, Cooper DR, Chruszcz M, Müller P, Sheldrick GM, et al. Validation of metal-binding sites in macromolecular structures with the CheckMyMetal web server. Nat Protoc. 2014; 9:156–170. https://doi.org/10.1038/nprot.2013.172 PMID: 24356774

32. Barbarino JM, Kroetz DL, Altman RB, Klein TE. PharmGKB summary: abacavir pathway. Pharmacogenet Genomics. 2014; 24:276–282. https://doi.org/10.1097/FPC.0000000000000040 PMID: 24625462

33. Miller WH, Miller RL. Phosphorylation of acyclovir (acycloguanosine) monophosphate by GMP kinase. J Biol Chem. 1980; 255:7204–7207. PMID: 6248551

34. Blaszczyk J, Li Y, Yan H, Ji X. Crystal structure of unligated guanylate kinase from yeast reveals GMP-induced conformational changes. J Mol Biol. 2001; 307:247–257. https://doi.org/10.1006/jmbi.2000.4427 PMID: 11243817

35. Sekulic N, Shuvalova L, Spangenberg O, Konrad M, Lavie A. Structural characterization of the closed conformation of mouse guanylate kinase. J Biol Chem. 2002; 277:30236–30243. https://doi.org/10.1074/jbc.M204668200 PMID: 12036965

36. Chen Y, Gallois-Montbrun S, Schneider B, Véron M, Moréra S, Deville-Bonne D, et al. Nucleotide binding to nucleoside diphosphate kinases: X-ray structure of human NDPK-A in complex with ADP and comparison to protein kinases. J Mol Biol. 2003; 332:915–926. https://doi.org/10.1016/j.jmb.2003.07.004 PMID: 12972261

37. Murakami E, Wang T, Babusis D, Lepist E-I, Sauer D, Park Y, et al. Metabolism and pharmacokinetics of the anti-hepatitis C virus nucleotide prodrug GS-6620. Antimicrob Agents Chemother. 2014; 58:1943–1951. https://doi.org/10.1128/AAC.02350-13 PMID: 24419340

38. Li J, Shi J, Xiao J, Tran L, Wang X, Zhu H-J. Contributions of Cathepsin A and Carboxylesterase 1 to the Hydrolysis of Tenofovir Alafenamide in the Human Liver, and the Effect of CES1 Genetic Variation

on Tenofovir Alafenamide Hydrolysis. Drug Metab Dispos. 2022; 50:243–248. https://doi.org/10.1124/dmd.120.000323 PMID: 34933885

39. Jumper J, Evans R, Pritzel A, Green T, Figurnov M, Ronneberger O, et al. Highly accurate protein structure prediction with AlphaFold. Nature. 2021; 596:583–589. https://doi.org/10.1038/s41586-021-03819-2 PMID: 34265844

40. Ferrer-Orta C, Arias A, Pérez-Luque R, Escarmís C, Domingo E, Verdaguer N. Sequential structures provide insights into the fidelity of RNA replication. Proc Natl Acad Sci U S A. 2007; 104:9463–9468. https://doi.org/10.1073/pnas.0700518104 PMID: 17517631

41. Tao Y, Farsetta DL, Nibert ML, Harrison SC. RNA synthesis in a cage—structural studies of reovirus polymerase lambda3. Cell. 2002; 111:733–745. https://doi.org/10.1016/s0092-8674(02)01110-8 PMID: 12464184

42. Malone B, Chen J, Wang Q, Llewellyn E, Choi YJ, Olinares PDB, et al. Structural basis for backtracking by the SARS-CoV-2 replication-transcription complex. Proc Natl Acad Sci U S A. 2021:118. https://doi.org/10.1073/pnas.2102516118 PMID: 33883267

43. Peersen OB. A Comprehensive Superposition of Viral Polymerase Structures. Viruses. 2019: 11. https://doi.org/10.3390/v11080745 PMID: 31412589

44. Freedman H, Winter P, Tuszynski J, Tyrrell DL, Houghton M. A computational approach for predicting off-target toxicity of antiviral ribonucleoside analogues to mitochondrial RNA polymerase. J Biol Chem. 2018; 293:9696–9705. https://doi.org/10.1074/jbc.RA118.002588 PMID: 29739852

45. Schwinghammer K, Cheung ACM, Morozov YI, Agaronyan K, Temiakov D, Cramer P. Structure of human mitochondrial RNA polymerase elongation complex. Nat Struct Mol Biol. 2013; 20:1298–1303. https://doi.org/10.1038/nsmb.2683 PMID: 24096365

46. Moréra S, Lacombe M-L, Yingwu X, Joël Janin GLA. X-ray structure of human nucleoside diphosphate kinase B complexed with GDP at 2 å resolution. Structure. 1995; 3:1307–1314. https://doi.org/10.1016/S0969-2126(01)00268-4 PMID: 8747457

47. Vonrhein C, Flensburg C, Keller P, Sharff A, Smart O, Paciorek W, et al. Data processing and analysis with the *autoPROC* toolbox. Acta Crystallogr D Biol Crystallogr. 2011; 67:293–302. https://doi.org/10.1107/S0907444911007773 PMID: 21460447

48. Vagin A, Teplyakov A. *MOLREP*: an Automated Program for Molecular Replacement. J Appl Crystallogr. 1997; 30:1022–1025. https://doi.org/10.1107/S0021889897006766

49. Smart OS, Sharff A, Holstein J, Womack TO, Flensburg C, Keller P, et al. Grade2 version 1.4.1. Cambridge, United Kingdom: Global Phasing Ltd; 2021.

50. Emsley P, Lohkamp B, Scott WG, Cowtan K. Features and development of Coot. Acta Crystallogr D Biol Crystallogr. 2010; 66:486–501. https://doi.org/10.1107/S0907444910007493 PMID: 20383002

51. Smart OS, Womack TO, Flensburg C, Keller P, Paciorek W, Sharff A, et al. Exploiting structure similarity in refinement: automated NCS and target-structure restraints in *BUSTER*. Acta Crystallogr D Biol Crystallogr. 2012; 68:368–380. https://doi.org/10.1107/S0907444911056058 PMID: 22505257

52. Krissinel E, Lebedev AA, Uski V, Ballard CB, Keegan RM, Kovalevskiy O, et al. CCP4 Cloud for structure determination and project management in macromolecular crystallography. Acta Crystallogr D Struct Biol. 2022; 78:1079–1089. https://doi.org/10.1107/S2059798322007987 PMID: 36048148

53. Murshudov GN, Skubák P, Lebedev AA, Pannu NS, Steiner RA, Nicholls RA, et al. REFMAC5 for the refinement of macromolecular crystal structures. Acta Crystallogr D Biol Crystallogr. 2011; 67:355–367. https://doi.org/10.1107/S0907444911001314 PMID: 21460454

54. Langer G, Cohen SX, Lamzin VS, Perrakis A. Automated macromolecular model building for X-ray crystallography using ARP/wARP version 7. Nat Protoc. 2008; 3:1171–1179. https://doi.org/10.1038/nprot.2008.91 PMID: 18600222

55. Winn MD, Ballard CC, Cowtan KD, Dodson EJ, Emsley P, Evans PR, et al. Overview of the CCP4 suite and current developments. Acta Crystallogr D Biol Crystallogr. 2011; 67:235–242. https://doi.org/10.1107/S0907444910045749 PMID: 21460441

56. Kabsch W. XDS. Acta Crystallogr D Biol Crystallogr. 2010; 66:125–132. https://doi.org/10.1107/S0907444909047337 PMID: 20124692

57. Evans PR, Murshudov GN. How good are my data and what is the resolution? Acta Crystallogr D Biol Crystallogr. 2013; 69:1204–1214. https://doi.org/10.1107/S0907444913000061 PMID: 23793146

58. McCoy AJ, Grosse-Kunstleve RW, Adams PD, Winn MD, Storoni LC, Read RJ. *Phaser* crystallographic software. J Appl Crystallogr. 2007; 40:658–674. https://doi.org/10.1107/S0021889807021206 PMID: 19461840

59. Long F, Nicholls RA, Emsley P, Graæulis S, Merkys A, Vaitkus A, et al. AceDRG: a stereochemical description generator for ligands. Acta Crystallogr D Struct Biol. 2017; 73:112–122. https://doi.org/10.1107/S2059798317000067 PMID: 28177307

60. Chen VB, Arendall WB, Headd JJ, Keedy DA, Immormino RM, Kapral GJ, et al. *MolProbity*: all-atom structure validation for macromolecular crystallography. Acta Crystallogr D Biol Crystallogr. 2010; 66:12–21. https://doi.org/10.1107/S0907444909042073 PMID: 20057044

61. Laskowski RA, MacArthur MW, Moss DS, Thornton JM. PROCHECK: a program to check the stereochemical quality of protein structures. J Appl Crystallogr. 1993; 26:283–291. https://doi.org/10.1107/S0021889892009944

62. Pettersen EF, Goddard TD, Huang CC, Couch GS, Greenblatt DM, Meng EC, et al. UCSF Chimera—a visualization system for exploratory research and analysis. J Comput Chem. 2004; 25:1605–1612. https://doi.org/10.1002/jcc.20084 PMID: 15264254

63. Cornell WD, Cieplak P, Bayly CI, Gould IR, Merz KM, Ferguson DM, et al. A Second Generation Force Field for the Simulation of Proteins, Nucleic Acids, and Organic Molecules. J Am Chem Soc. 1995; 117:5179–5197. https://doi.org/10.1021/ja00124a002

64. Hinsen K, Petrescu A-J, Dellerue S, Bellissent-Funel M-C, Kneller GR. Harmonicity in slow protein dynamics. Chem Phys. 2000; 261:25–37. https://doi.org/10.1016/S0301-0104(00)00222-6

65. Lindorff-Larsen K, Piana S, Palmo K, Maragakis P, Klepeis JL, Dror RO, et al. Improved side-chain torsion potentials for the Amber ff99SB protein force field. Proteins. 2010; 78:1950–1958. https://doi.org/10.1002/prot.22711 PMID: 20408171

66. Trott O, Olson AJ. AutoDock Vina: Improving the speed and accuracy of docking with a new scoring function, efficient optimization, and multithreading. J Comput Chem. 2010; 31:455–461. https://doi.org/10.1002/jcc.21334 PMID: 19499576

67. Meng EC, Goddard TD, Pettersen EF, Couch GS, Pearson ZJ, Morris JH, et al. UCSF ChimeraX: Tools for structure building and analysis. Protein Sci. 2023; 32:e4792. https://doi.org/10.1002/pro.4792 PMID: 37774136